

Realization of Vertically Aligned, Ultrahigh Aspect Ratio InAsSb Nanowires on Graphite

E. A. Anyebe,[†] A. M. Sanchez,[‡] S. Hindmarsh,[‡] X. Chen,[§] J. Shao,[§] M. K. Rajpalke,^{||} T. D. Veal,^{||} B. J. Robinson,[†] O. Kolosov,[†] F. Anderson,[⊥] R. Sundaram,[⊥] Z. M. Wang,^{*,#} V. Falko,[†] and Q. Zhuang^{*,†}

[†]Physics Department, Lancaster University, Lancaster LA1 4YB, U.K.

[‡]Department of Physics, Warwick University, Coventry CV4 7AL, U.K.

[§]National Laboratory for Infrared Physics, Shanghai Institute of Technical Physics, Chinese Academy of Sciences, 200083 Shanghai, People's Republic of China

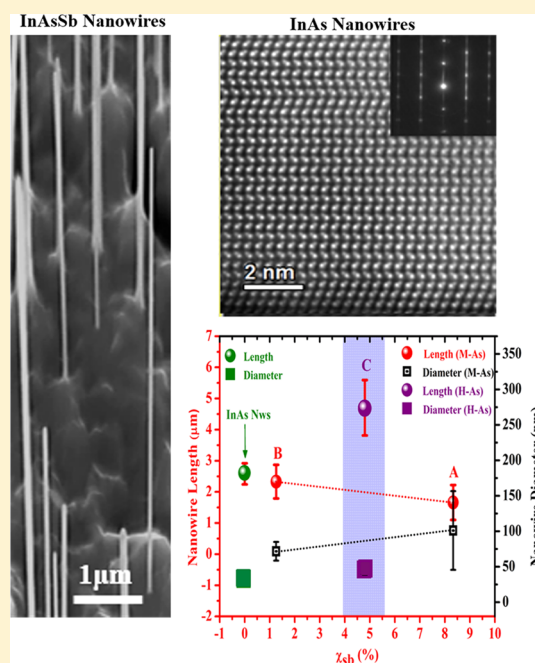
^{||}Stephenson Institute for Renewable Energy and Department of Physics, University of Liverpool, Liverpool L69 7ZF, U.K.

[⊥]Oxford Instruments, Tubney Woods, Abingdon OX13 5QX, U.K.

[#]Institute of Fundamental and Frontier Sciences, University of Electronic Science and Technology of China, Chengdu 610054, People's Republic of China

Supporting Information

ABSTRACT: The monolithic integration of InAs_{1-x}Sb_x semiconductor nanowires on graphitic substrates holds enormous promise for cost-effective, high-performance, and flexible devices in optoelectronics and high-speed electronics. However, the growth of InAs_{1-x}Sb_x nanowires with high aspect ratio essential for device applications is extremely challenging due to Sb-induced suppression of axial growth and enhancement in radial growth. We report the realization of high quality, vertically aligned, nontapered and ultrahigh aspect ratio InAs_{1-x}Sb_x nanowires with Sb composition ($x_{\text{Sb}}(\%)$) up to $\sim 12\%$ grown by indium-droplet assisted molecular beam epitaxy on graphite substrate. Low temperature photoluminescence measurements show that the InAs_{1-x}Sb_x nanowires exhibit bright band-to-band related emission with a distinct redshift as a function of Sb composition providing further confirmation of successful Sb incorporation in as-grown nanowires. This study reveals that the graphite substrate is a more favorable platform for InAs_{1-x}Sb_x nanowires that could lead to hybrid heterostructures possessing potential device applications in optoelectronics.



KEYWORDS: InAsSb, nanowire, self-catalyzed, molecular beam epitaxy, van der Waals, aspect ratio, graphite, graphene

InAs_{1-x}Sb_x materials have long been recognized as highly suitable candidates for infrared photodetectors since it possess the narrowest bandgap energy among all the III-V semiconductors (0.1 eV at room temperature).¹ Therefore, the InAs_{1-x}Sb_x tunable band gap would cover the two most important atmospheric infrared windows, i.e., 3–5 and 8–12 μm . This enables a number of important applications such as industrial and pollution monitoring (e.g., CO₂, CH₄, N₂O, O₃, and CO gases),^{2–4} surveillance, health, and security. InAs_{1-x}Sb_x infrared photodetectors (PDs) have attracted enormous research interest as a potential alternative to current state-of-the-art CdHgTe-based detectors, which suffer from costly

growth and processing, nonuniformity⁵ and toxicity concerns.⁶ Semiconductor nanowires (NWs) offer the possibility to significantly improve the sensitivity of PDs owing to their ultrasensitivity, low power consumption, and fast response⁷ evidenced by the demonstration of highly sensitive NWs based detectors.^{8,9} Specifically, thin and long NWs, i.e., high aspect ratio (AR), would significantly improve the sensing characteristics of PDs due to their larger effective surfaces.^{10,11} Such NW

Received: January 31, 2015

Revised: June 6, 2015

Published: June 18, 2015

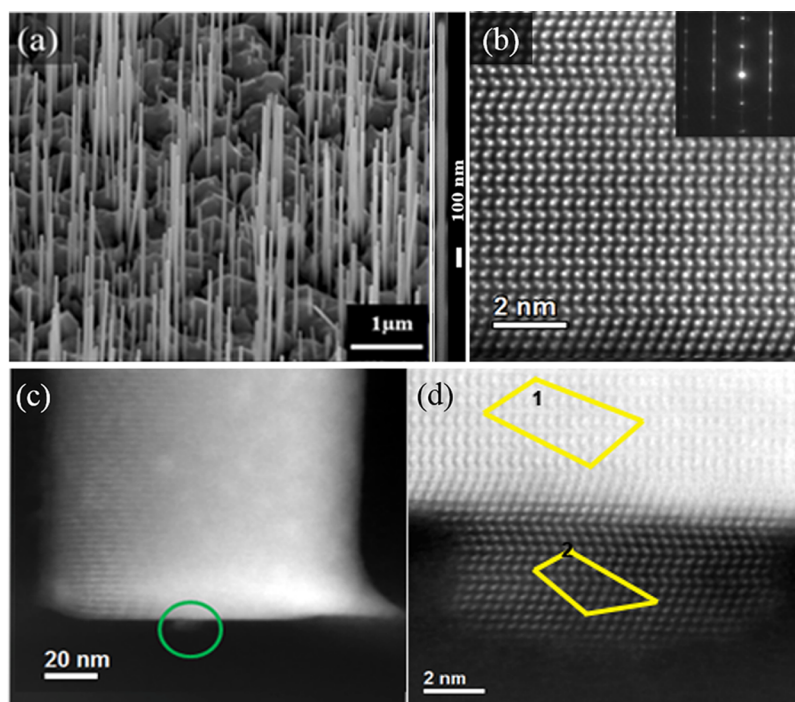


Figure 1. (a) A 45° tilted SEM image of dense, high aspect ratio InAs nanowires grown on graphite substrate by MBE. (b) ADF-TEM image of an InAs NW demonstrating the coexistence of ZB and WZ structures. (c) ADF image showing a small “seed” of material just underneath the NW into the graphitic substrate (green circle). (d) High magnification ADF of the seed and the base of the nanowires. The areas where EDX analysis was carried out are indicated in yellow.

materials also enable investigation of other important material related properties such as spin–orbit coupling and quantum confinement.

In addition, the monolithic integration of high AR InAs_{1-x}Sb_x NWs on graphitic substrates (GS) holds promise for the development of high performance, flexible, and cost-effective functional devices. In such hybrid architectures, the two-dimensional graphene substrate can function as an ideal electrode because of its high transparency, high conductance, and excellent chemical stability.^{12,13} Over the past few years, several graphene-based devices including light emitting diodes,¹⁴ transistors,^{15,16} solar cells,^{17,18} supercapacitor,¹⁹ nanogenerator,²⁰ photodetector,²¹ and gas detector²² have been reported. Furthermore, GS are ideal platforms for NW growth via van der Waals (VDW) epitaxy due to the absence of dangling bonds.^{23–25} Binary InP and GaP,²⁶ GaAs,^{26,27} and ZnO^{28,29} NWs have been demonstrated on GS. InAs NWs/GS hybrid structures has also been synthesized though was limited to Au-catalyzed molecular beam epitaxy (MBE)²⁶ or self-catalyzed metal–organic vapor phase epitaxy (MOVPE).^{23–25} Recently, we reported the MBE growth of InAs NWs on GS,³⁰ but the NWs exhibited a low AR and areal density. In addition, the growth of ternary compound alloys on GS has been focused on InGaAs alloys.^{17,25} To date, InAs_{1-x}Sb_x NW growth has only been demonstrated on Si.^{31–33} However, these studies revealed that InAs_{1-x}Sb_x NWs generally have a low AR due to the surfactant effect of antimony (Sb), which suppresses axial growth while promoting radial expansion.^{31,32,34}

In this letter, we demonstrate for the first time, the self-catalyzed growth of ultrahigh AR InAs_{1-x}Sb_x NWs on GS. Although the InAs_{1-x}Sb_x NWs on the graphitic platform also show an expansion in radial dimension and suppression of axial growth with increased Sb content, we observed that the Sb-

induced modifications in NWs geometry is dramatically less in comparison to that on Si. Through optimizing growth conditions, we successfully obtained InAs_{1-x}Sb_x NWs with ultrahigh AR up to 100:1. The optical properties of InAsSb NWs with different Sb composition (up to $x_{\text{Sb}(\%)} = 12\%$) are also presented.

High AR InAs NWs were first realized on the GS at As-rich conditions by MBE for a growth duration of 60 min via an In-assisted growth technique³⁵ (more details in Methods). Scanning electron microscope (SEM) image of the InAs NWs in Figure 1a reveals a uniform NW diameter along the entire length with no visible tapering (see inset). The NWs have an estimated length (L_{NW}) of $2.58 \pm 0.34 \mu\text{m}$, diameter (D_{NW}) of $31.2 \pm 6.6 \text{ nm}$ and density of $8.09 \times 10^8 \text{ cm}^{-2}$ showing a high AR of ~ 83 . This corresponds to over three times increase in NW AR compared to previously reported self-catalyzed MBE grown InAs NWs/graphite.³⁰ This significant improvement is attributed to the well optimized growth conditions. The SEM image also reveals that the NWs grown on GS are vertically well-aligned with a high degree of size uniformity evidenced by the small standard deviation both in L_{NW} and D_{NW} . This superior NWs morphology represents a considerable improvement in the geometry and density compared to that of previously reported Au²⁶ and self-catalyzed MOCVD grown InAs NWs on GS^{23–25} with diameters in the range of $\sim 40\text{--}87 \text{ nm}$ and density of $(2\text{--}7) \times 10^8 \text{ cm}^{-2}$. The high yield of vertically well-aligned InAs NWs (InAs[111]||graphite[0001]) could be attributed to the nearly coherent in-plane lattice matching between InAs $\langle 110 \rangle$ and graphene $\langle 1000 \rangle$.^{23,24,27} High resolution annular dark field (ADF) scanning transmission electron microscope (STEM) images (see Figure 1b) of an InAs/GS indicates that the NWs are composed of mixed zinc blende (ZB) and wurtzite (WZ)

phases³⁰ (polytypism). This is consistent with previous reports of self-catalyzed InAs NWs.^{36,37} The polytypic nature of the NWs was also confirmed by the electron diffraction pattern (inset of Figure 1b). The multiple stacking faults on the (111)_{ZB}/(0001)_{WZ} planes produce the streaks in the diffraction pattern. This behavior is related to the lower surface energy of the WZ phase compared to the ZB phase, which results in a more stable WZ phase in NWs structures.³⁸ Aiming to gain insight into the structure of the graphite–InAs NWs interface, a focused ion beam (FIB) specimen containing both NW on the graphitic substrate was analyzed. High resolution ADF-STEM images (see Figure 1c) demonstrated a small “seed” of material just underneath the NW into the graphitic substrate (which is brighter than the substrate and marked with a green circle in the image), i.e., it seems the NW is pinned to the substrate. EDX spectra were carried out in areas 1 and 2 (yellow areas in Figure 1d). The atomic composition areas 1 and 2 were 48% In–52% As and 49% In–51% As, respectively. Therefore, the “seed” is InAs, which originated during the initial growth stage; In droplets deposited in the graphitic substrate are subsequently converted into InAs in the presence of excess As. This seed acts as nucleation site to initiate NW growth.

In order to elucidate the conditions for realizing high AR InAs_{1-x}Sb_x NWs, a series of samples were grown on GS by MBE. The growths were performed under moderately As-rich (M-As) conditions (samples A and B) and highly As-rich (H-As) conditions (sample C) (see Methods for growth details). The Sb composition ($x_{\text{Sb}}(\%)$) in the NWs was controlled by varying the Sb fractional flux (Ψ_{R}) in the range of 1.64–2.93% [where Ψ_{R} represents the ratio of Sb flux (Ψ_{Sb}) to the overall group V ($\Psi_{\text{As}} + \Psi_{\text{Sb}}$) fluxes]. X-ray diffraction (XRD) and energy-dispersive X-ray spectroscopy (EDX) measurements were used to determine the Sb composition in the InAs_{1-x}Sb_x NWs. Figure 2 shows that two diffraction peaks are present in all samples. The one at 26.5° is indexed to graphite (002), and the other at a lower diffraction angle is associated with the (111) ZB InAs_{1-x}Sb_x. Compared to the InAs ZB (111) peak at

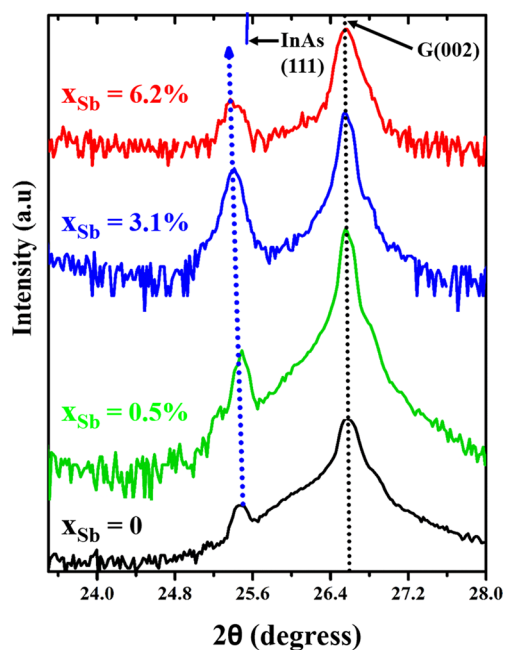


Figure 2. X-ray diffraction patterns of InAs_{1-x}Sb_x nanowires grown on graphite with different Sb compositions.

25.4°,³⁹ the diffraction peak of (111) InAs_{1-x}Sb_x NWs shifts to lower angles with increase of Sb composition. Based on an assumption of Vegard’s law⁴⁰ and full relaxation, the Sb composition ($x_{\text{Sb}}(\%)$) was deduced to be 6.2%, 0.5%, and 3.1% for samples A–C, respectively. Due to the formation of parasitic islands during the growth (see Figure 1a), there is likelihood of contribution from the islands to the diffraction peaks in the XRD measurements. In order to confirm the presence of Sb in the NWs and determine the content more precisely, we performed EDX measurements in SEM on all the samples. To ensure validity and consistency of the measurements, several EDX measurements were taken, e.g., measured on the NWs from side (tilted 45°) along the NWs at different positions near the bottom and the tip as well as top view images. All of these measurements gave quite consistent values (see Figures S1 and S2 in Supporting Information for further details) and also close to the values deduced from XRD measurements (summarized in Table 1). These measurements

Table 1. Growth Parameters for a Series of Samples of InAs_{1-x}Sb_x Nanowires Grown on Graphite and Si(111) Substrates

| sample | substrate | series | growth time (min) | Sb fractional flux (Ψ_{R}) | Sb content (%) (XRD) | Sb content (%) (EDX) |
|--------|-----------|-------------------|-------------------|--|----------------------|----------------------|
| A | graphite | M-As ^a | 120 | 1.64 | 6.2 | 8 |
| B | graphite | M-As | 120 | 2.93 | 0.5 | 1 |
| C | graphite | H-As ^b | 120 | 1.82 | 3.1 | 5 |
| D | silicon | M-As | 120 | 2.93 | 0.5 | 2 |
| E | silicon | M-As | 120 | 4.68 | 11.1 | 7 |
| F | silicon | H-As | 120 | 1.82 | 4.7 | 4 |

^aModerately As-rich conditions. ^bHighly As-rich conditions.

confirm the presence of Sb in the NWs. To further verify Sb composition in the NWs as well as exclude any possibility of contributions from the parasitic islands, thickness of sample, the substrate and geometry such as tilt and detector position, and EDX measurements were also performed in TEM. Figure 3a,b shows the bright field images of typical InAs_{1-x}Sb_x NWs (samples A and B, respectively). EDX spectra in TEM mode were taken along the length of the NWs. The measured Sb content in the samples A and B was ~8% and ~1%, respectively, with a slight variation along the NW length. Please note that we provided only two decimals for the resulting composition deduced from EDX. This is due to the unknown uncertainties of the nominal Cliff–Lorimer k -factors used in the quantification calculation though the material thickness and its density are known reasonably well. The EDX spectra in EDX-TEM also show that the Sb compositions closely correlate with the EDX-SEM and XRD data, which implies the Sb incorporation is quite close in both NW growth and parasitic growth. We therefore adopt the average of EDX deduced data for this work with the Sb content determined from the average Sb composition taken along the different positions of the tilted NWs and top view images. It is worth noting that the X-ray deduced compositions are generally less than that determined from EDX measurements. This disparity could be attributed to the modification of the phases in the presence of Sb as previously observed.³³

Figure 4a,b shows the representative low and high magnification SEM images of InAs_{1-x}Sb_x NWs grown on GS within the M-As regime. The NWs exhibit a 6-fold symmetry

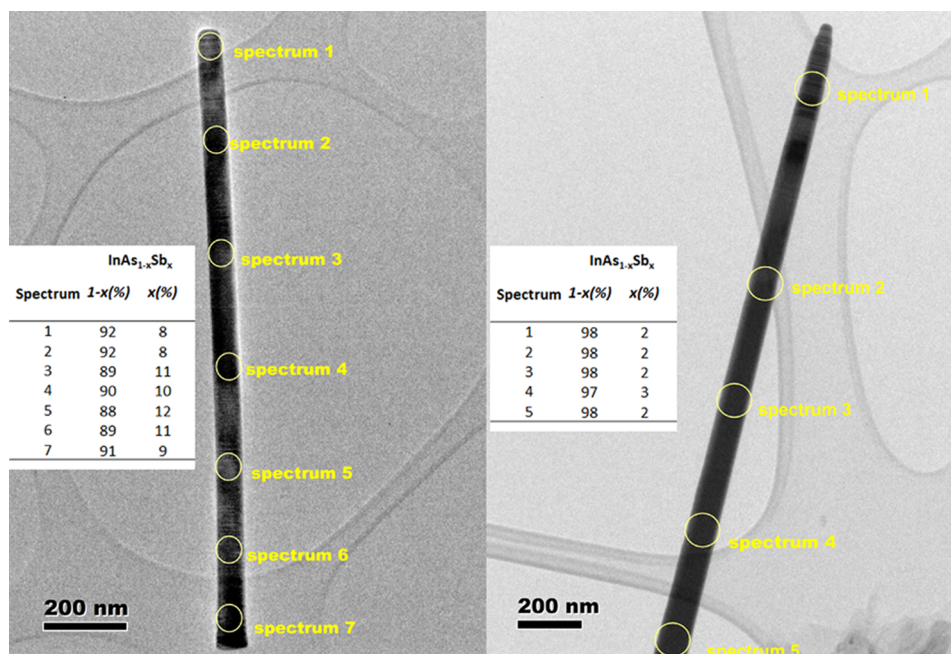


Figure 3. Representative bright field TEM images and position of EDX spectra to deduce the Sb composition ($x_{\text{Sb}(\%)}$) along the NW length for samples with (a) high Sb composition and (b) low Sb composition.

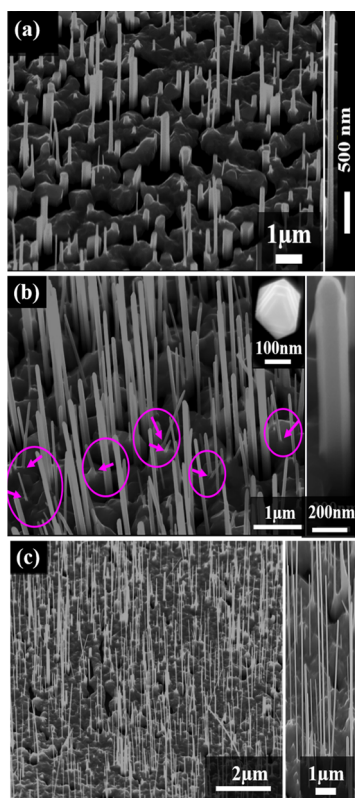


Figure 4. Images of 45° tilted low and high magnification SEM of InAs_{1-x}Sb_x nanowire samples of A, B, and C grown on graphite at moderately As-rich (a,b) and highly As-rich (c) with Sb compositions of 8%, 1%, and 5%, respectively. The inset shows a top view image of the NW.

(inset of Figure 4b) of the side facets characteristic of NWs growing along the $\langle 111 \rangle_{\text{B}}$ direction. Analysis of the SEM images reveals that the NWs are ~ 72 – 101 nm thick and ~ 1.7 – 2.3 μm long. No In droplet is present at the NW tip, which can

be attributed to their consumption under excess As flux. Figure 4c shows the SEM image of sample C, grown in the H-As regime (i.e., higher As-flux), while the In-flux and Ψ_{R} (1.82%) are comparable to that of sample A (Table 1). It reveals a high yield of NWs with an average density of $1.46 \times 10^8 \text{ cm}^{-2}$, typical length of $\sim 4.70 \pm 0.89 \mu\text{m}$, and diameter of $\sim 46.0 \pm 6.9$ nm. In addition, this optimal growth condition led to a high yield of vertically well-aligned and nontapered NWs (highly uniform diameter along the entire length). The side-view close-up image of a representative NW (inset Figure 4c) shows no diameter broadening or wire bending along the entire length despite the high AR. This is a distinct signature of morphologically superior NWs. Figure 5 reveals the strong dependence of the NWs geometry, aspect ratio, and density on Sb composition ($x_{\text{Sb}(\%)}$). The NWs length (L_{NW}) and diameter (D_{NW}) as a function of $x_{\text{Sb}(\%)}$ is plotted in Figure 5a. A total NW population of ~ 150 NWs was utilized for the calculation of NWs density while employing Gaussian approximations; $>70\%$ of measurable NWs were used for the determination of the error bars of the NWs geometry (L_{NW} and D_{NW}), which is expressed as the deviation from the mean geometry of normally distributed NWs. The data for the InAs NWs on graphite is also shown for comparison. The monotonic decrease in L_{NW} and expansion of D_{NW} with increasing Sb content within the M-As regime clearly indicates a suppression of axial NWs growth with a corresponding enhancement in radial growth. This is consistent with previous reports^{31–33} and is attributed to Sb surfactant effect. In sharp contrast, the H-As conditions promote axial NW growth evidenced by the large L_{NW} and small D_{NW} as exhibited in sample C. The observed trend is more evident in Figure 5b, which shows the dependence of NW AR on $x_{\text{Sb}(\%)}$. As can be seen, the samples grown within the M-As regime show a monotonic decrease in AR with a maximum of ~ 32 for sample B ($x_{\text{Sb}(\%)}$ = 1%). Such a behavior is attributed to the Sb-induced modifications in thermodynamic and kinetic processes.³¹ The InAs NWs are relatively longer and thinner than all the M-AR samples with an AR of ~ 83 , even though

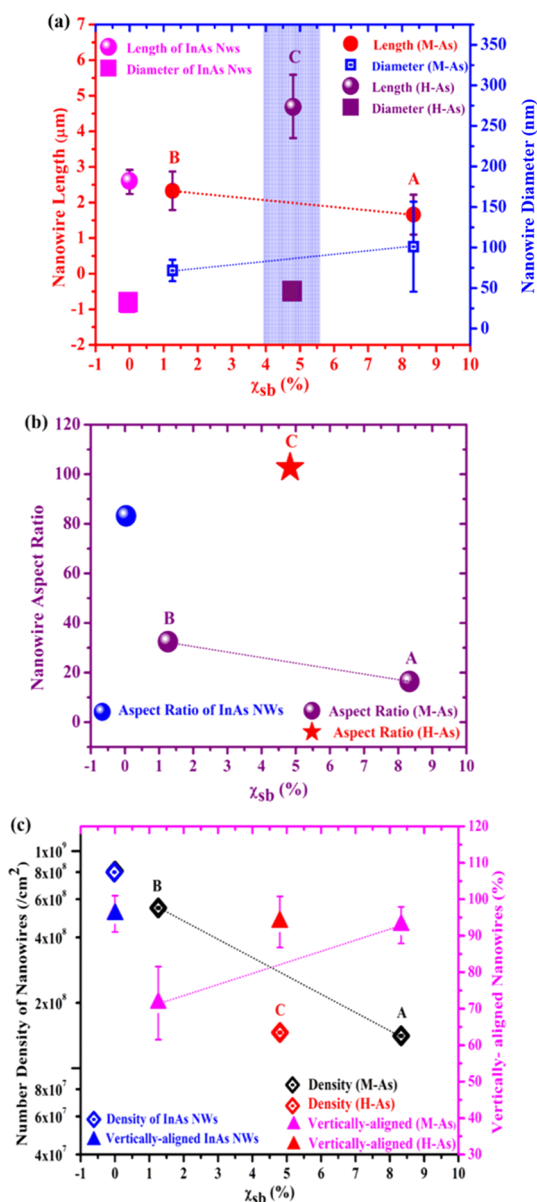


Figure 5. Measured $\text{InAs}_{1-x}\text{Sb}_x$ nanowire (a) length (L_{NW}) and diameter (D_{NW}); (b) aspect ratio and (c) number density and fraction of vertically aligned nanowires (%) as a function of Sb content ($x_{\text{Sb}}(\%)$) for moderately As-rich (M-As) and highly As-rich (H-As) samples. Sample names are also shown.

they were grown for only 60 min (half the duration of the M-AR samples). Intriguingly, NWs with exceptionally high AR (~ 102) were obtained in sample C, which was grown within the H-As regime (over $3\times$ the maximum AR of the M-As samples) despite the relatively high Sb content ($x_{\text{Sb}}(\%) = 5\%$). It has been previously reported^{32,41} that trace Sb concentration induces an increase in radial growth with a suppression of axial growth leading to the growth of short and thick NWs. This trend is clearly different from the observations reported in a previous study,³¹ which demonstrated that the introduction of small amount of Sb (4%) induces a significant increase in radial growth. Consequently, the observed high AR of sample C can be correlated to an enhancement in axial growth resulting from the availability of excess As flux. To further explore the effect of As-rich conditions on the AR of droplet-assisted NWs on GS, a series of InAs NWs samples were grown on graphite at varying

As-fluxes (see Methods for growth details). At a relatively low As-flux, no NW growth was obtained; however, an increase in As-flux (As-rich conditions) resulted in the growth of NWs. Further increase in As-flux promoted axial NW growth, which is evidenced by the significant increase in AR (see Figure S4 in Supporting Information). This indicates that As-rich condition favors the growth of high AR NWs on the GS which is similar to a previous report.⁴² It has recently been demonstrated that the elongation rate of self-catalyzed NWs is highly dependent on the group V flux.^{43,44} As a result, the radial NW growth promoted at moderately As-rich condition due to the surfactant effect of Sb can be inhibited by employing significantly high As-flux. Also, Sb incorporation has a significant effect on NW density (Figure 5c). Compared to the high yield of InAs NWs, the density of $\text{InAs}_{1-x}\text{Sb}_x$ NWs was significantly reduced with an increase in Sb composition ($x_{\text{Sb}}(\%)$). This is attributed to the reduced NW nucleation probability due to the enhanced lateral growth³² and the increased nucleation barrier, which results from a lowering of the interfacial energy with increased Sb content.²⁶ An evaluation of sample A (Figure 4a) reveals that the resulting NWs are nonuniform in both length and diameter. This suggests the onset of the evolution from 3D NWs to 2D thin film in the presence of 8% Sb. Sb incorporation in InAs generally favors the growth of a dominant 2D film due to a kinetically inhibited In adatom mobility³¹ in the presence of Sb. Surfactant Sb is known to delay 2D \rightarrow 3D growth mode transition while promoting layer by layer growth,⁴⁵ as demonstrated by Copel et al.⁴⁶ They showed that trace Sb content could induce a change in growth mode. To further validate our inference on the suppression of radial growth by As-rich conditions and to elucidate the superiority of the graphitic substrate for InAsSb NW growth, we evaluated the morphology of $\text{InAs}_{1-x}\text{Sb}_x$ NWs grown on bare Si(111) substrates at identical conditions to that on the GS (see Methods for growth details). Samples D and F on Si were grown with identical conditions as samples B and C (on GS), respectively, and sample E was grown under M-AR conditions with a high Sb fractional flux (Ψ_{R}) of 4.68. The Sb compositions were determined by EDX-SEM analysis (see Figure S3 in Supporting Information) to be 2%, 7%, and 4% in samples D, E, and F, respectively (Table 1). It is a surprise that the Sb incorporation ($x_{\text{Sb}}(\%)$) in the NWs scales inversely with the Sb fractional flux (Ψ_{R}) for $\Psi_{\text{R}} \leq 2.93$ on both Si and GS. Incidentally, this corresponds to the region within which NW growth was realized. For instance, sample B contain less Sb in the NWs despite the higher Sb flux compared with that of Sample A. This abnormal behavior could be associated with the Sb surfactant effect,³¹ which is more pronounced in NW structures owing to their high surface to volume ratio. The higher Ψ_{R} increases Sb surface coverage, results in increased Sb segregation and surface site blocking,⁴⁷ and thereby reduces the incorporation probability and composition of Sb in the NWs. A disproportionate Sb incorporation has previously been reported in the literature.^{31,48} A similar behavior was demonstrated by Sourribes et al.³³ It was shown that the Sb composition monotonically increases with an increase in Ψ_{R} in the range of 0–1.31%, while a slight increase in Ψ_{R} (1.53%) led to a decline in Sb composition. However, it is worth noting that this behavior could be highly dependent on growth conditions and growth mode. For instance, the 2D growth of sample E resulted in higher Sb composition at increased Ψ_{R} ($\Psi_{\text{R}} = 4.68$, $x_{\text{Sb}}(\%) = 7\%$). The SEM images of as-grown $\text{InAs}_{1-x}\text{Sb}_x$ NWs on Si are shown in Figure S5 in Supporting Information. We observed

that an increase of Sb composition reduced the NW areal density for the NWs grown on Si (Figure 6). This dependence

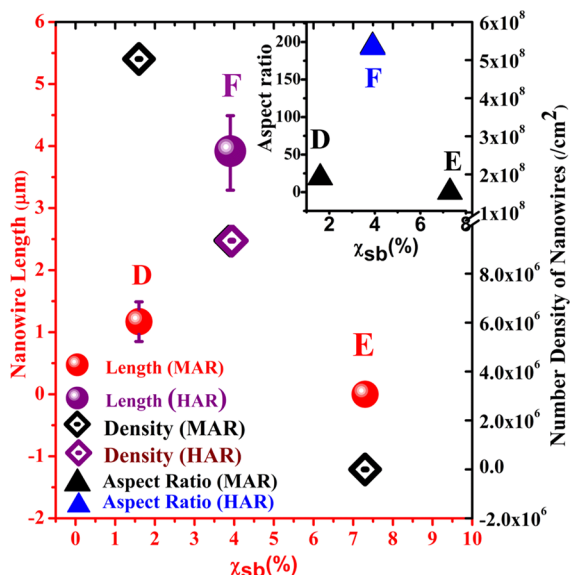


Figure 6. Plot of the dependence of length and density (in log scale) of nanowires grown on Si(111) as a function of Sb composition ($x_{\text{Sb}(\%)}$). Sample names are also shown.

is indicative of Sb-induced quenching of NWs nucleation probability, which is similar to the observation in the NWs grown on GS. The presence of 7% Sb completely suppressed NW growth on Si (sample E). The plot of L_{NW} as a function of x_{Sb} (Figure 6) indicates a suppression of axial NW growth with increased x_{Sb} for the samples grown within the M-As regime, which is consistent with the $\text{InAs}_{1-x}\text{Sb}_x/\text{GS}$ samples. However, the NWs on GS are relatively longer than the ones on Si. At Ψ_{R} of 2.9%, the NWs on Si are only about 1.17 μm long (sample D, $x_{\text{Sb}(\%)} = 2\%$), while the corresponding NWs on GS (sample B) is almost double that length ($\sim 2.33 \mu\text{m}$). Similarly, for the samples grown with excess As-flux (H-As), at Ψ_{R} of 1.82%, NWs of $\sim 3.89 \mu\text{m}$ long were obtained on Si (sample F, $x_{\text{Sb}(\%)} = 4\%$) while $\sim 4.70 \mu\text{m}$ long NWs were obtained on GS (sample C, $x_{\text{Sb}(\%)} = 5\%$). This suggests that GS favors the growth of high AR NWs in comparison to that on Si possibly due to differences in adatom mobility. It has been shown theoretically and experimentally that the axial growth rate of MBE grown NWs is strongly dependent on adatom diffusion from the substrate to the droplet but not so strongly on adsorption on the drop.^{49,50} We recently demonstrated that the elongation rate of In-catalyzed NWs is significantly influenced by adatom diffusion from the side facets to the droplet.^{30,31,35} Consequently, any slight variation in adatom diffusion length owing to the changes along the substrate would translate to significant variations in axial growth rate and hence the NWs aspect ratio. In addition, among the NW samples on Si, sample F exhibits the highest AR (inset of Figure 6) although it has a relatively high Sb content ($x_{\text{Sb}(\%)} = 4\%$), which is again associated with the H-As condition that favors axial growth. This corroborates the observed dependence of NWs AR on As-flux and further confirms that highly As-rich conditions are essential for the suppression of radial growth in favor of enhanced axial growth in $\text{InAs}_{1-x}\text{Sb}_x$ NWs.

We also investigated the percentage of vertically aligned NWs grown on GS as a function of x_{Sb} (Figure 5c). A low yield

of vertically aligned NWs was obtained in sample B ($x_{\text{Sb}(\%)} = 1\%$) (see also the SEM image in Figure 4b) compared to the other $\text{InAs}_{1-x}\text{Sb}_x$ NWs samples (A and C) on graphite. To clarify the effect of the GS on the vertical directionality of NWs, we evaluated the morphology of sample D grown on Si at identical growth conditions to sample B. The SEM image indicates a high yield ($\sim 95\%$) of vertically well-aligned NWs was realized on Si (refer to Figure S5a in Supporting Information). This suggests that the observed high density of randomly aligned NWs in sample B (on GS) could be attributed to the influence of the graphitic substrate. A close evaluation of the SEM image for sample B reveals that the unaligned NWs grew on the islands (see Figure 4b signified by arrows). Mohseni et al.²⁵ observed a similar growth of nonvertical NWs on islands, which themselves preferentially grew along graphene line defects. It is likely that the rough sections on the GS promote the formation of large and dense InAs islands, which in turn mitigates the epitaxial growth of NWs on the GS and is in agreement with previous report.²⁴

Finally, in order to investigate the optical properties of InAsSb NWs/graphite, low temperature (10 K) photoluminescence (PL) was performed on a Fourier transform infrared (FTIR) spectrometer (Bruker Vertex 80v), which runs in the step-scan mode. A Kr^+ -ion laser operating at a 647 nm spectral line was used to excite the samples. PL signal was detected by a liquid-nitrogen cooled HgCdTe detector with a lock-in amplifier. The detailed setup has been reported previously.⁵¹ Figure 7 shows the PL spectra of three samples

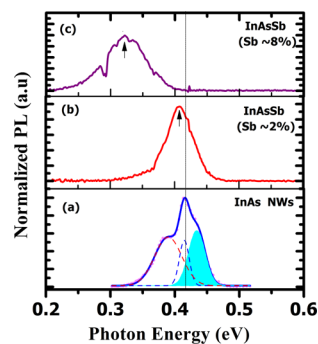


Figure 7. Low temperature (10 K) photoluminescence spectra of (a) InAs NWs and $\text{InAs}_{1-x}\text{Sb}_x$ NWs with Sb composition ($x_{\text{Sb}(\%)}$) of (b) $\sim 2\%$ and (c) $\sim 12\%$ grown on graphite substrate.

with Sb composition of 0, $\sim 2\%$, and $\sim 12\%$. The sample of pure InAs NWs exhibits three emission peaks centered at ~ 0.389 , 0.415, and 0.434 eV, which have been associated with impurity-related transition, type II alignment transition, and band-to-band (BtB) transition, respectively, due to the polytypic nature of the NWs, e.g., the phase mixture of WZ and ZB.⁵² The sample of $\text{InAs}_{0.98}\text{Sb}_{0.02}$ NWs shows a strong emission centered at 0.406 eV with a weak shoulder emission peaked at 0.442 eV, which originate from BtB transition of ZB and WZ InAsSb , respectively. The sample of $\text{InAs}_{0.88}\text{Sb}_{0.12}$ NWs shows one emission at 0.323 eV. Given a bowing effect of 0.67 eV,¹ InAsSb alloy at low temperature for Sb composition of 2% and 12% gives bandgap energy of 0.400 and 0.324 eV, which are very close to the dominant peak emission present in the samples of $\text{InAs}_{0.98}\text{Sb}_{0.02}$ NWs (0.406 eV) and $\text{InAs}_{0.88}\text{Sb}_{0.12}$ NWs (0.323 eV), respectively. These spectra clearly show the redshift of the emission related to Sb incorporation due to bandgap shrinkage. It should be noted that type II related emission could possibly

contribute to the dominant emission from the $\text{InAs}_{1-x}\text{Sb}_x$ samples due to the polytypic nature of the NWs. Detailed PL measurements at varied temperature and laser excitation power are ongoing to clarify other possible origins and to understand the optical evolution with Sb incorporation. The shoulder emission at 0.442 eV in the sample of $\text{InAs}_{0.98}\text{Sb}_{0.02}$ NWs could be associated with the BtB transition of WZ InAsSb , which has higher bandgap energy than that of ZB $\text{InAs}_{0.98}\text{Sb}_{0.02}$ NWs by 42 meV. This is in good agreement with previous studies of InAs NWs (46 meV).⁵³ A previous report indicates that the WZ phase InAs NWs has larger bandgap energy in comparison with that of ZB InAs ,^{53–55} at a predicted value of 40–66 meV.^{54,56,57} This was confirmed with an experimentally observed value of ~ 0.46 eV⁵³). In addition, these PL spectra also show an increase of line width with the increase of Sb incorporation. This is attributed to the nonuniform Sb distribution across the NWs. However, the mechanism leading to this nonuniformity in Sb composition is unclear and requires further study. However, due to the presence of InAsSb parasitic clusters/islands on the Si surface, they can possibly contribute to the PL emissions. In order to clarify there are no contributions from the islands to the observed PL emission, PL measurements were performed on $\text{InAs}_{1-x}\text{Sb}_x/\text{GS}$ NW samples. All the NWs were removed from substrates leaving behind only the islands and PL measurements taken. No PL emission was detected. The nonemission is associated with the poor material quality of the clusters resulting from the large lattice mismatch and antiphase domains. These measurements demonstrate that the observed PL emission indeed originates from InAsSb NWs ensembles.

In summary, we have demonstrated for the first time, the self-catalyzed growth of dense, vertically aligned, and high aspect ratio $\text{InAs}_{1-x}\text{Sb}_x$ NWs on graphitic substrate by molecular beam epitaxy. Sb-induced radial NWs expansion coupled with axial growth suppression results in the growth of short and thick NWs at moderately As-rich conditions. Such modification in morphology is significantly reduced by growing NWs on GS platform. We also demonstrated that highly As-rich condition enables the realization of ultrahigh aspect ratio NWs. Photoluminescence measurements demonstrate a distinct redshift in the band-to-band related emission with increasing Sb composition confirming the presence of Sb in as-grown nanowires. Our study elucidates a promising technique for the monolithic integration of $\text{InAs}_{1-x}\text{Sb}_x$ NWs on graphitic thin films for high-performance, flexible, and cost-effective optoelectronic devices.

Methods. $\text{InAs}_{1-x}\text{Sb}_x$ NWs samples were grown on graphite substrate by MBE. The graphitic films were mechanically exfoliated from highly oriented pyrolytic graphite (HOPG) and transferred onto Si(111) substrates and subsequently loaded into the system and outgassed for over 2 h. Prior to NW growth, the substrates were activated by optimal indium (In) droplets³⁵ with a diameter of ~ 70 nm to facilitate NW nucleation. The substrates were then warmed up to 420–500 °C while keeping the In source closed followed by the simultaneous introduction of all growth precursors using a fixed In beam equivalent pressure (BEP). Moderately As-rich (M-As) samples (A and B) were grown with an As-flux in the range of 10^{-6} mbar, while sample C was grown in a highly As-rich (H-As) regime using a higher As-flux in the range of 10^{-5} mbar. A series of M-As (D and E) and H-As (F) InAsSb NW samples were also grown on bare Si(111) substrates at identical conditions to the corresponding $\text{InAs}_{1-x}\text{Sb}_x$ NWs/graphite

samples. Prior to NW growth, the Si substrates were chemically cleaned by 12% HF solutions for 4 min to remove the native oxide and quickly loaded into the MBE system to avoid reoxidation, then thermally outgassed. The InAs NW sample was deposited on the graphite at M-As conditions for a growth duration of 60 min and temperatures of 420–500 °C. In order to investigate the influence of As-flux on NW aspect ratio, a set of InAs NWs samples were grown on graphite at a constant temperature for 20 min growth duration. The In BEP was fixed, while the As-flux was varied in the range of $(2-8) \times 10^{-6}$ mbar. The surface morphology of as-grown NWs was investigated by FEI XL30 SFEG scanning electron microscope (SEM) with an energy-dispersive X-ray spectroscopy (EDX) for composition determination. X-ray diffraction (XRD) measurements were performed on a Philips PW 1720. High-resolution transmission electron microscope (HRTEM) and annular dark field (ADF) scanning transmission electron microscopy (STEM) images were taken in a JEOL-JEM 2100 and ARM-200F microscopes both working at 200 kV. Focused ion beam (FIB) specimens were prepared using a JIB4500 to investigate the interface with the substrate. EDX measurements were carried out with an Oxford Instrument X-MAX 80.

■ ASSOCIATED CONTENT

📄 Supporting Information

Further details of SEM images of InAs nanowires on graphite and $\text{InAs}_{1-x}\text{Sb}_x$ NWs on Si (111) as well as energy dispersive X-ray spectroscopy (EDX) spectra of $\text{InAs}_{1-x}\text{Sb}_x$ NWs on graphite and Si (111) substrates. The Supporting Information is available free of charge on the ACS Publications website at DOI: 10.1021/acs.nanolett.5b00411.

■ AUTHOR INFORMATION

Corresponding Authors

*E-mail: q.zhuang@lancaster.ac.uk.

*E-mail: zhmwang@gmail.com.

Notes

The authors declare no competing financial interest.

■ ACKNOWLEDGMENTS

The authors would like to thank the EPSRC Lancaster Impact Acceleration Account and Gas Sensing Solutions for their financial support.

■ REFERENCES

- (1) Vurgaftman, I.; Meyer, J. R.; Ram-Mohan, L. R. *J. Appl. Phys.* **2001**, *89*, 5815–5875.
- (2) Thelander, C.; Caroff, P.; Plissard, S.; Dick, K. A. *Appl. Phys. Lett.* **2012**, *100*, 232105.
- (3) Yen, M. Y.; People, R.; Wecht, K. W.; Cho, A. Y. *Appl. Phys. Lett.* **1988**, *52*, 489–491.
- (4) Borg, B. M.; Dick, K. A.; Eymery, J.; Wernersson, L.-E. *Appl. Phys. Lett.* **2011**, *98*, 113104.
- (5) Rogalski, A. *Prog. Quantum Electron.* **2003**, *27*, 59–210.
- (6) Pea, M.; Ercolani, D.; Li, A.; Gemmi, M.; Rossi, F.; Beltram, F.; Sorba, L. *J. Cryst. Growth* **2013**, *366*, 8–14.
- (7) Chen, X.; Wong, C. K. Y.; Yuan, C. A.; Zhang, G. *Sens. Actuators, B* **2013**, *177*, 178–195.
- (8) Liao, L.; Lu, H. B.; Shuai, M.; Li, J. C.; Liu, Y. L.; Liu, C.; Shen, Z. X.; Yu, T. *Nanotechnology* **2008**, *19*, 175501.
- (9) Guo, J.; Zhang, J.; Zhu, M.; Ju, D.; Xu, H.; Cao, B. *Sens. Actuators, B* **2014**, *199*, 339–345.
- (10) Liao, L.; Lu, H. B.; Li, J. C.; He, H.; Wang, D. F.; Fu, D. J.; Liu, C.; Zhang, W. F. *J. Phys. Chem. C* **2007**, *111*, 1900–1903.

- (11) Baxter, J. B.; Walker, A. M.; Ommering, K. V.; Aydil, E. S. *Nanotechnology* **2006**, *17*, S304–S312.
- (12) Huang, X.; Zeng, Z.; Fan, Z.; Liu, J.; Zhang, H. *Adv. Mater.* **2012**, *24*, 5979–6004.
- (13) Kim, H.; Bae, S. H.; Han, T. H.; Lim, K. G.; Ahn, J. H.; Lee, T. W. *Nanotechnology* **2014**, *25*, 014012.
- (14) Tchernycheva, M.; Layenus, P.; Zhang, H.; Babichev, A. V.; Jacopin, G.; Shahmohammadi, M.; Julien, F. H.; Ciecchonski, R.; Vescovi, G.; Kryliouk, O. *Nano Lett.* **2014**, *14*, 2456–2465.
- (15) Liao, L.; Lin, Y. C.; Bao, M. Q.; Cheng, R.; Bai, J. W.; Liu, Y. A.; Qu, Y. Q.; Wang, K. L.; Huang, Y.; Duan, X. F. *Nature* **2010**, *467*, 305–308.
- (16) Hwang, J. O.; Lee, D. H.; Kim, J. Y.; Han, T. H.; Kim, B. H.; Park, M.; No, K.; Kim, S. O. *J. Mater. Chem.* **2011**, *21*, 3432–3437.
- (17) Mohseni, P. K.; Behnam, A.; Wood, J. D.; Zhao, X.; Yu, K. J.; Wang, N. C.; Rockett, A.; Rogers, J. A.; Lyding, J. W.; Pop, E.; Li, X. *Adv. Mater.* **2014**, *26*, 3755–3760.
- (18) Seo, K. W.; Lee, J. H.; Cho, N. G.; Kang, S. J.; Kim, H. K.; Na, S. I.; Koo, H. W.; Kim, T. W. *J. Vac. Sci. Technol., A* **2014**, *32*, 061201.
- (19) Perera, S. D.; Rudolph, M.; Mariano, R. G.; Nijem, N.; Ferraris, J. P.; Chabal, Y. J.; Balkus, K. J. *Nano Energy* **2013**, *2*, 966–975.
- (20) Choi, D.; Choi, M. Y.; Choi, W. M.; Shin, H. J.; Park, H. K.; Seo, J. S.; Park, J.; Yoon, S. M.; Chae, S. J.; Lee, Y. H.; Kim, S. W.; Choi, J. Y.; Lee, S. Y.; Kim, J. M. *Adv. Mater.* **2010**, *22*, 2187–2192.
- (21) Miao, J.; Hu, W.; Guo, N.; Lu, Z.; Liu, X.; Liao, L.; Chen, P.; Jiang, T.; Wu, S.; Ho, J. C.; Wang, L.; Chen, X.; Lu, W. *Small* **2015**, *11*, 936–942.
- (22) Quang, V. V.; Dung, N. V.; Trong, N. S.; Hoa, N. D.; Duy, N. V.; Hieu, N. V. *Appl. Phys. Lett.* **2014**, *105*, 013107.
- (23) Hong, Y. J.; Lee, W. H.; Wu, Y.; Ruoff, R. S.; Fukui, T. *Nano Lett.* **2012**, *12*, 1431–1436.
- (24) Hong, Y. J.; Fukui, T. *ACS Nano* **2011**, *5*, 7576–7584.
- (25) Mohseni, P. K.; Behnam, A.; Wood, J. D.; English, C. D.; Lyding, J. W.; Pop, E.; Li, X. L. *Nano Lett.* **2013**, *13*, 1153–1161.
- (26) Wallentin, J.; Kriegner, D.; Stangl, J.; Borgström, M. T. *Nano Lett.* **2014**, *14*, 1707–1713.
- (27) Munshi, A. M.; Dheeraj, D. L.; Fauske, V. T.; Kim, D. C.; Van Helvoort, A. T. J.; Fimland, B. O.; Weman, H. *Nano Lett.* **2012**, *12*, 4570–4576.
- (28) Kumar, B.; Lee, K. Y.; Park, H.-K.; Chae, S. J.; Lee, Y. H.; Kim, S.-W. *ACS Nano* **2011**, *5*, 4197–4204.
- (29) Kim, Y.-J.; Lee, J.-H.; Yi, G.-C. *Appl. Phys. Lett.* **2009**, *95*, 213101.
- (30) Zhuang, Q.; Anyebe, E. A.; Sanchez, A. M.; Rajpalke, M. K.; Veal, T. D.; Zhukov, A.; Robinson, B. J.; Anderson, F.; Kolosov, O.; Falko, V. *Nanoscale Res. Lett.* **2014**, *9*, 321.
- (31) Anyebe, E. A.; Rajpalke, M. K.; Veal, T. D.; Jin, C. J.; Wang, Z. M.; Zhuang, Q. *Nano Res.* **2015**, *8*, 1309–1319.
- (32) Du, W.-N.; Yang, X.-G.; Wang, X.-Y.; Pan, H.-Y.; Ji, H.-M.; Luo, S.; Yang, T.; Wang, Z.-G. *J. Cryst. Growth* **2014**, *396*, 33–37.
- (33) Sourribes, M. J. L.; Isakov, I.; Panfilova, M.; Liu, H.; Warburton, P. A. *Nano Lett.* **2014**, *14*, 1643–1650.
- (34) Ercolani, D.; Gemmi, M.; Nasi, L.; Rossi, F.; Pea, M.; Li, A.; Salviati, G.; Beltram, F.; Sorba, L. *Nanotechnology* **2012**, *23*, 115606.
- (35) Anyebe, E. A.; Zhuang, Q.; Sanchez, A.; Lawson, S.; Robson, A. J.; Ponomarenko, L.; Zhukov, A.; Kolosov, O. *Phys. Status Solidi RRL* **2014**, *8*, 658–662.
- (36) Wei, W.; Bao, X.-Y.; Soci, C.; Ding, Y.; Wang, Z.-L.; Wang, D. *Nano Lett.* **2009**, *9*, 2926–2934.
- (37) Dimakis, E.; Lähnemann, J.; Jahn, U.; Breuer, S.; Hulse, M.; Geelhaar, L.; Riechert, H. *Cryst. Growth Des.* **2011**, *11*, 4001–4008.
- (38) Johansson, J.; Dick, K. A.; Caroff, P.; Messing, M. E.; Bolinsson, J.; Deppert, K.; Samuelson, L. *J. Phys. Chem. C* **2010**, *114*, 3837–3842.
- (39) *Powder Diffraction File 65–6115*; The International Centre for Diffraction Data (ICDD): Newtown Square, PA, 1994.
- (40) Vegard, L. *Z. Phys.* **1921**, *5* (1), 17–26.
- (41) Plissard, S. R.; Slapak, D. R.; Verheijen, M. A.; Hocevar, M.; Immink, G. W. G.; van Weperen, I.; Nadj-Perge, S.; Frolov, S. M.; Kouwenhoven, L. P.; Bakkers, E. P. A. M. *Nano Lett.* **2012**, *12*, 1794–1798.
- (42) Babu, J. B.; Yoh, K. J. *Cryst. Growth* **2011**, *323*, 301–303.
- (43) Glas, F.; Ramdani, M. R.; Patriarche, G.; Harmand, J. C. *Phys. Rev. B: Condens. Matter* **2013**, *88*, 195304.
- (44) Ramdani, M. R.; Harmand, J. C.; Glas, F.; Patriarche, G.; Travers, L. *Cryst. Growth Des.* **2013**, *13*, 91–96.
- (45) Portavoce, A.; Berbezier, I.; Ronda, A. *Mater. Sci. Eng. B* **2003**, *101*, 181–185.
- (46) Copel, M.; Reuter, M. C.; van Hoegen, M. H.; Tromp, R. M. *Phys. Rev. B: Condens. Matter* **1990**, *42*, 11682–11689.
- (47) Nimmatoori, P.; Zhang, Q.; Dickey, E. C.; Redwing, J. M. *Nanotechnology* **2009**, *20*, 025607.
- (48) Anyebe, E. A.; Zhuang, Q. *Mater. Res. Bull.* **2014**, *60*, 572–575.
- (49) Dubrovskii, V. G.; Cirlin, G. E.; Soshnikov, I. P.; Tonkikh, A. A.; Sibirev, N. V.; Samsonenko, Y. B.; Ustinov, V. M. *Phys. Rev. B: Condens. Matter* **2005**, *71*, 205325.
- (50) Dubrovskii, V. G.; Sibirev, N. V.; Harmand, J. C.; Glas, F. *Phys. Rev. B: Condens. Matter* **2008**, *78*, 235301–10.
- (51) Shao, J.; Lu, C. X.; Lu, W.; Lu, X.; Zhu, L. W.; Guo, S.; He, L.; Chu, J. *Appl. Phys. Lett.* **2010**, 121915.
- (52) Zhuang, Q. D.; Anyebe, E. A.; Chen, R.; Liu, H.; Sanchez, A. M.; Rajpalke, M. K.; Veal, T. D.; Wang, Z. M.; Huang, Y. Z.; Sun, H. D. *Nano Lett.* **2015**, *15*, 1109–116.
- (53) Moeller, M.; De Lima, M. M., Jr.; Cantarero, A.; Chieramonte, T.; Cotta, M. A.; Iikawa, F. *Nanotechnology* **2012**, *23*, 375704.
- (54) Zanolli, Z.; Fuchs, F.; Furthmueller, J.; von Barth, U.; Bechstedt, F. *Phys. Rev. B: Condens. Matter* **2007**, *75*, 245121–8.
- (55) Bao, J.; Bell, D. C.; Capasso, F.; Erdman, N.; Wei, D.; Froberg, L.; Martensson, T.; Samuelson, L. *Adv. Mater.* **2009**, *21*, 3654–8.
- (56) Murayama, M.; Nakayama, T. *Phys. Rev. B: Condens. Matter* **1994**, *49*, 4710–24.
- (57) De, A.; Pryor, C. E. *Phys. Rev. B: Condens. Matter* **2011**, *84*, 155210–13.